MATERIALS PHYSICS AND MECHANICS RESEARCH ARTICLE

**Submitted: July 3, 2026** **Revised: July 23, 2026** **Accepted: August 14, 2026**

# Effect of silicon microalloying on microstructure and HVOF spraying behavior of AlCrFeCoNi high-entropy alloy coating

**E.V. Volokitina** ✉, **D.V. Masaylo, A.E. Kim, A.A. Popovich**

Peter the Great St. Petersburg Polytechnic University, St. Petersburg, Russia

✉ volokitina1606@gmail.com

**ABSTRACT**

This study investigates the effect of 0.11 wt. % Si microalloying on AlCrFeCoNi high-entropy alloy coatings produced via mechanical alloying and HVOF spraying. Optimal milling times were 7.5 h for the base alloy and 10 h for the Si-modified one. Spark plasma sintering revealed mixed Body-Centered Cubic and Face-Centered Cubic structures with silicide precipitates. Preliminary abrasive wear tests indicated a tendency for surface stabilization in the Si-modified alloy due to tribo-oxide films. Crucially, during HVOF, Si preferentially oxidized, shielding Cr from burnout (17.64 vs. 14.16 % in the base coating) and significantly improving coating adhesion by eliminating through-cracking, forming a monolithic structure.

**KEYWORDS**

high-entropy alloys • mechanical alloying • plasma spheroidization • high-velocity oxygen-fuel spraying

***Funding***. *The research was carried out with the financial support of the Ministry of Science and Higher Education within the framework of the Strategic Academic Leadership program "Priority 2030" (Agreement No. 075-15-2026-097 dated April 3, 2026).*

**Citation:** Volokitina EV, Masaylo DV, Kim AE, Popovich AA. Effect of silicon microalloying on microstructure and HVOF spraying behavior of AlCrFeCoNi high-entropy alloy coating. *Materials Physics and Mechanics*. 2026;54(4): 34–43.
http://dx.doi.org/10.18149/MPM.5442026_4

## Introduction

In recent decades, high-entropy alloys (HEAs) have established themselves as a revolutionary class of structural and functional materials [1–3]. Due to the effects of high entropy, sluggish diffusion, lattice distortion, and the "cocktail" effect, HEAs exhibit a unique combination of strength, thermal stability, and potential for surface-protection applications [4–7]. Recent studies also confirm their outstanding creep resistance and long-term strength at elevated temperatures, which is critical for load-bearing structures [8].

Among the variety of HEA systems, alloys based on AlCoCrFeNi attract particular attention due to the possibility of purposeful control of the phase composition [9,10]. Varying the aluminum content allows the formation of structures with a predominance of the ductile FCC (Face-Centered Cubic) phase or hard BCC (Body-Centered Cubic) phase, as well as two-phase eutectic compositions that provide an optimal balance of hardness and toughness [11–14]. However, to achieve maximum tribological characteristics, the introduction of alloying additives is often required. In particular, it has been shown that microalloying with non-metals such as silicon promotes dispersion strengthening due to the formation of silicides, and also stimulates the formation of protective oxide layers on the friction surface, reducing the friction coefficient and wear rate [15–17].

Thermal spraying, in particular the high-velocity oxygen-fuel (HVOF) method, is a cost-effective and scalable method for applying wear-resistant coatings without loss of

© E.V. Volokitina, D.V. Masaylo, A.E. Kim, A.A. Popovich, 2026.
Publisher: Peter the Great St. Petersburg Polytechnic University
This is an open access article under the CC BY-NC 4.0 license (https://creativecommons.org/li-censes/by-nc/4.0/)

substrate toughness [18,19]. At the same time, thermal spraying methods and subsequent structural modification of coatings make it possible to significantly increase their wear resistance and durability in friction units [20]. Nevertheless, the application of HVOF for HEAs is associated with a number of problems: high-temperature oxidation of particles in the flame leads to changes in the chemical composition of the coating, and high thermal stresses can cause cracking and delamination [21,22]. Systematic studies of the effect of microalloying on the behavior of HEAs during gas-flame spraying, in particular on oxidation kinetics and adhesive strength, remain insufficiently studied.

This work aims to study the effect of silicon microalloying on the kinetics of mechanical alloying, phase composition, microstructure, and tribological properties of coatings from the AlCrFeCoNi alloy obtained by HVOF spraying.

## Materials and Methods

The selection of the investigated compositions AlCrFeCoNi and $AlCrFeCoNiSi_{0.01}$ is based on the analysis of literature data and thermodynamic modeling of phase diagrams in Thermo-Calc software based on the Calphad method. Elemental metal powders with a purity of 99.96% were used as initial components, which were mixed in an inert atmosphere (the ratio of components is presented in Table 1).

**Table 1.** Component ratio

| Composition | Al, wt.% | Cr, wt.% | Fe, wt.% | Co, wt.% | Ni, wt.% | Si, wt.% |
|---|---|---|---|---|---|---|
| AlCrFeCoNi | 10.69 | 20.60 | 22.12 | 23.34 | 23.25 | 0 |
| $AlCrFeCoNiSi_{0.01}$ | 10.68 | 20.57 | 22.10 | 23.32 | 23.22 | 0.11 |

Mechanical alloying (MA) was performed in a Fritsch Pulverisette 4 planetary ball mill with a main disk rotation speed of 200 rpm, planets rotation speed of 400 rpm, and a ball-to-powder mass ratio of 20:1. MA was carried out in hard alloy jars, using hard alloy balls as grinding media, the process was carried out in an inert argon atmosphere, sampling was performed after 5, 7.5, and 10 h of MA. 1 wt. % of isopropyl alcohol was added as a grinding agent.

Particle size was investigated using a Fritsch Analysette 22 Nano Tecplus laser diffractometer. Powder compaction to study mechanical properties and structure was performed by spark plasma sintering (SPS) using an HPD 25 FCT Systeme G unit. The powder was placed in a graphite die with a diameter of 20 mm, heated to a temperature of 1100 °C at a rate of 100 °C/min, after which a pressure of 50 MPa was applied and held for 3 min. The sintering process was carried out in vacuum.

The true density of the compact SPS samples was experimentally determined using helium gas pycnometry with a Densi 100 instrument. Measurements were performed at room temperature using high-purity helium (99.999 %) as the penetrating gas, which ensures accurate determination of the skeletal (true) volume of the material by penetrating open micropores inaccessible to liquid-based methods. Prior to the measurements, the samples were degassed under vacuum to remove adsorbed moisture and surface contaminants.

Plasma spheroidization was performed on a Tekna TEK 15 unit with the following parameters: power 15 kW, pressure 1 atm, sheath gas (Ar) 35 slpm, central gas (Ar)

10 slpm, option gas ($H_2$ 4 slpm, carrier gas (Ar) 5 slpm, and feed rate 21.5 g/min. Coatings were applied to low-carbon steel substrates by high-velocity oxygen-fuel spraying on a UC-1000 APS + HVOF Spray System thermal spraying unit. Oxygen consumption 900 l/min, O/F 1.16, kerosene consumption 24 l/h, spraying distance 350 mm, number of passes 4, robot movement speed 200 mm/s, powder feed rate 50 g/min.

The phase composition was investigated using a Bruker D8 Advance diffractometer in copper Kα radiation ($\lambda$ = 0.15418 nm). Further processing of diffraction data was performed by the Rietveld method using BRUKER Diffrac Plus Topas software. The structure of the samples was investigated on ground and polished samples using a Mira 3 Tescan Scanning Electron Microscopy (SEM) with an Energy Dispersive X-ray Spectroscopy (EDS) attachment (Oxford Instruments X-Max 80) for X-ray energy dispersive microanalysis.

Microhardness was determined by the Vickers method on a Buehler microhardness tester with a load of 200 g; at least 5 measurements were performed for statistics. Wear resistance was investigated in accordance with the ASTM G65 standard[1] (Procedure B) for dry sand/rubber wheel abrasion testing. The physical essence of this method is the simulation of low-stress 3-body abrasive wear, where standardized silica sand is continuously fed into the gap between a rotating neoprene rubber wheel and the stationary sample surface under a specified load (130 N), causing micro-cutting and micro-plowing of the material. The total wear distance was 2872 m (4000 wheel revolutions), divided into two equal cycles to evaluate both the running-in and steady-state wear behavior. Prior to each weighing, the samples were carefully cleaned of loose abrasive particles and wear debris in strict accordance with the ASTM G65 protocol. Mass loss was measured using analytical balances with a precision of ± 0.0001 g. Despite the limitation in sample quantity, ASTM G65 (Procedure B) was specifically chosen over two-body methods (e.g., pin-on-disk) because it uniquely simulates low-stress three-body abrasion, which is the dominant failure mechanism for hard metallic coatings in real-world industrial applications. This standard provides a more relevant physical model of micro-cutting by loose abrasive particles, even though it inherently requires larger wear volumes for strict statistical validation.

## Results and Discussion

Figure 1(a,b) shows SEM images of the AlCrFeCoNi powder after 7.5 and 10 h of MA without the addition of isopropanol. The process is characterized by the predominance of cold welding, which leads to the formation of a pronounced layered structure with a low degree of homogenization. The introduction of 1 wt. % of isopropanol made it possible to balance the processes of welding and destruction. After 5 h of MA (Fig. 1(c)), there are unalloyed particles of pure components in the structure. By 7.5 h (Fig. 1(d)), complete homogenization is achieved, the layering disappears. A further increase in time to 10 h (Fig. 1(e)) does not lead to significant morphological changes.

[1] American Society for Testing and Materials. Standard ASTM G65-16. *Standard Test Method for Measuring Abrasion Using the Dry Sand/Rubber Wheel Apparatus.* ASTM International; 2021.

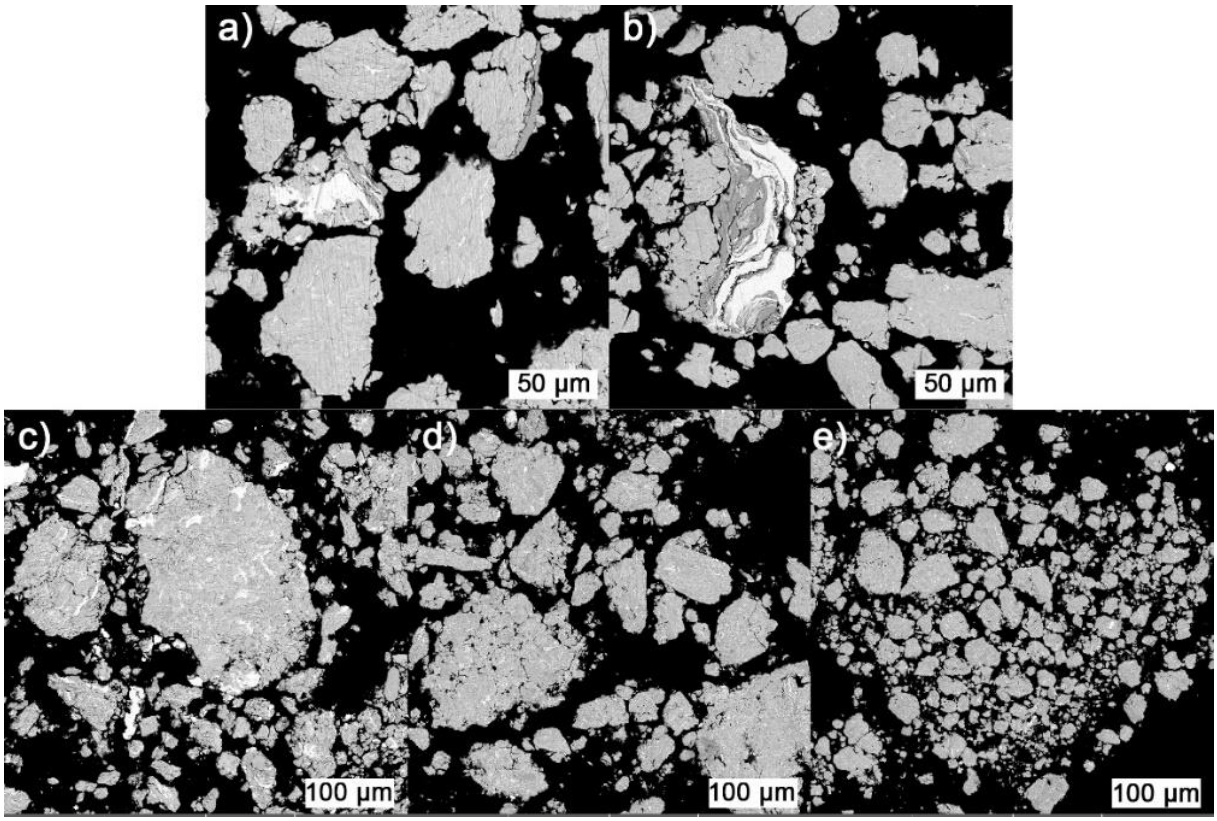



**Fig. 1.** Microstructure of AlCrFeCoNi powder: (a) 7.5 h MA without isopropanol, (b) 10 h MA without isopropanol, (c) 5 h MA with isopropanol, (d) 7.5 h MA with isopropanol, (e) 10 h MA with isopropanol

Analysis of the particle size distribution (Fig. 2(a)) confirms these observations. After 5 h of MA, the distribution is bimodal ($d_{10}$ = 9.36 μm, $d_{50}$ = 44.75 μm, $d_{90}$ = 98.9 μm), which indicates agglomeration. At 7.5 h, the distribution becomes unimodal with a narrow peak ($d_{50}$ = 31.9 μm), indicating the achievement of dynamic equilibrium. At 10 h, some peak broadening is observed ($d_{50}$ = 28.0 μm) due to over-grinding.

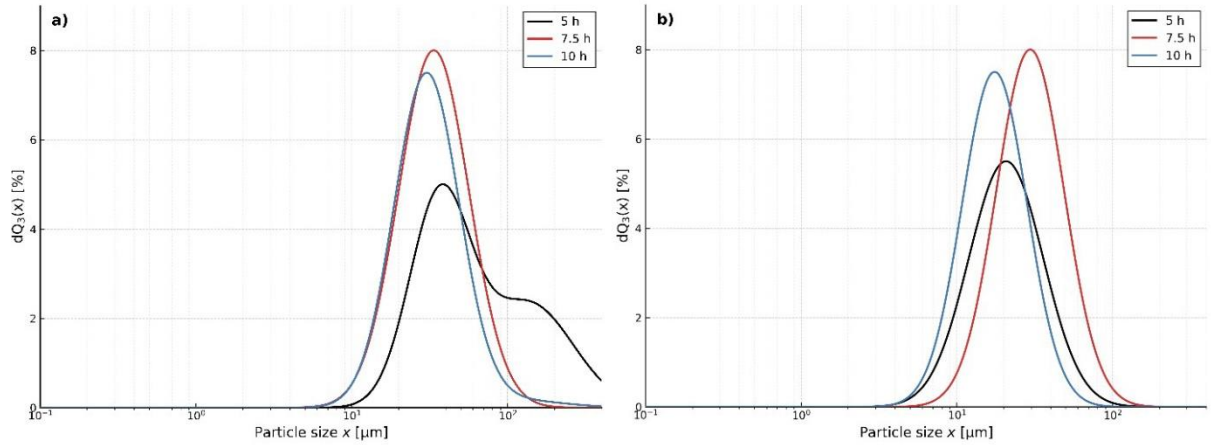



**Fig. 2.** Particle size distribution depending on MA duration: (a) AlCrFeCoNi, (b) $AlCrFeCoNiSi_{0.01}$

For the $AlCrFeCoNiSi_{0.01}$ composition, the alloying kinetics turned out to be different (Figs. 2(b) and 3). The presence of silicon probably slows down the diffusion processes due to the formation of intermediate refractory compounds. After 5 h of MA, there are

separate particles of pure elements in the structure. Complete homogenization is achieved only by 10 h of MA, while the particle size distribution remains narrow and suitable for spheroidization ($d_{50}$ = 23.1 μm vs. 19.3 μm at 10 h without Si).

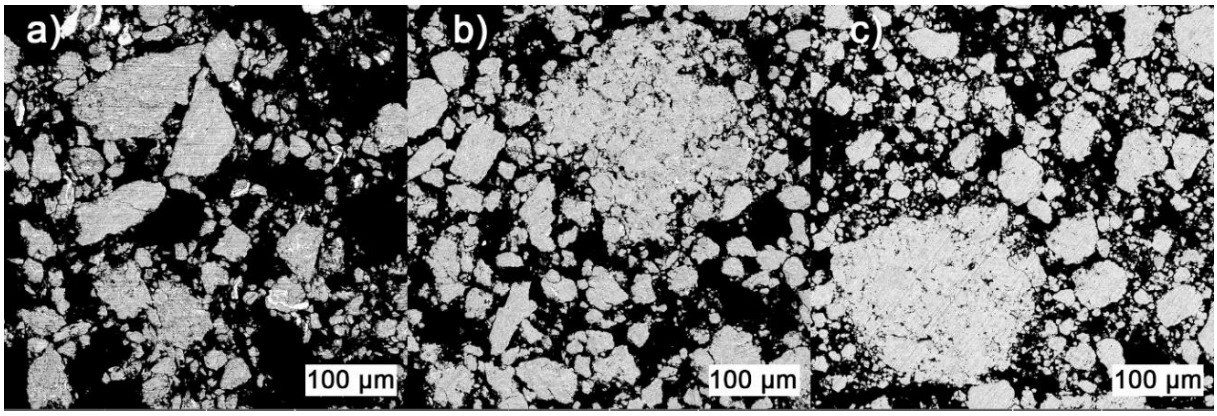



**Fig. 3.** Microstructure of $AlCrFeCoNiSi_{0.01}$: (a) 5h MA, (b) 7.5h MA, (c) 10h MA

The average chemical composition of the AlCrFeCoNi powders obtained after 7.5 and 10 h of MA with the addition of isopropyl alcohol is presented in Table 2. When comparing the obtained results with the initial component ratio, the powder after 7.5 h of MA has the closest chemical composition; however, there is a slight excess of iron and a deficiency of nickel. In the powder after 10 h, there is a chromium deficiency of more than 2 wt. %, a nickel deficiency, and an excess of iron. It should be noted that when analyzing statistical data on the chemical composition, the powder after 7.5 h of MA is characterized by a narrower spread of component content than after 10 h. Table 2 also presents the average chemical composition of $AlCrFeCoNiSi_{0.01}$ powders after 7.5 and 10 h of MA. When compared with the initial component ratio, the powder after 10 h of MA is closer in chemical composition; there is a slight deficiency of nickel, which is compensated by small increases in the other alloy components. The EDS analysis results confirm that 7.5 h is optimal for AlCrFeCoNi (the composition is closest to the calculated one, the spread is minimal), and 10 h for $AlCrFeCoNiSi_{0.01}$.

**Table 2.** Average content of components in alloys

| Powder | Al, wt. % | Si, wt. % | Cr, wt. % | Fe, wt. % | Co, wt. % | Ni, wt. % |
|---|---|---|---|---|---|---|
| AlCrFeCoNi, 7.5 h | 10.73 | - | 20.22 | 24.01 | 23.71 | 21.34 |
| AlCrFeCoNi, 10 h | 10.82 | - | 18.25 | 24.21 | 23.81 | 22.90 |
| $AlCrFeCoNiSi_{0.01}$, 7 5 h | 11.51 | 0.23 | 19.12 | 23.34 | 23.57 | 22.23 |
| $AlCrFeCoNiSi_{0.01}$, 10 h | 10.93 | 0.21 | 20.47 | 22.15 | 23.36 | 22.60 |

Investigation of the samples after SPS (Fig. 4(a,b)) showed that the structure of AlCrFeCoNi consists of a light phase (enriched in Ni), which predominates in the volume of the sample, and a dark phase (enriched in Cr). The introduction of Si does not change the morphology radically; however, fine precipitates, presumably silicides, are observed along the grain boundaries, and the contrast and amount of the light phase also decrease.

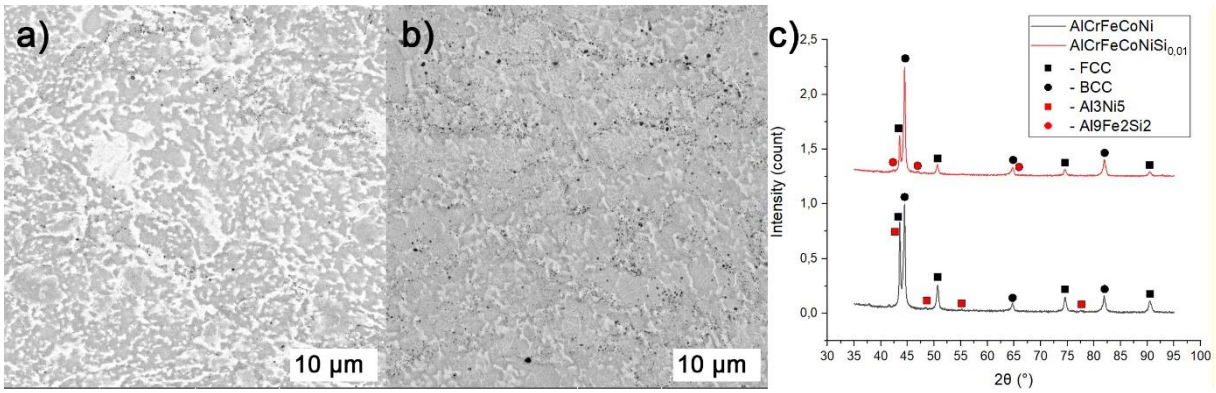



**Fig.4.** SEM images of the structure of sintered samples: (a) AlCrFeCoNi, (b) $AlCrFeCoNiSi_{0.01}$, (c) XRD patterns of sintered samples

XRD analysis (Fig. 4(c)) revealed that both alloys consist of solid solutions based on BCC and FCC lattices. In the AlCrFeCoNi alloy, the FCC phase predominates; weak peaks of the $Al_3Ni_5$ intermetallic compound are present. In the modified alloy, the intensity of the FCC phase peaks decreases, which indicates its stabilization in smaller volumes, and the silicide phase $Al_9Fe_2Si_2$ is additionally identified.

The chemical composition of the samples showed insignificant fluctuations in composition and is characterized by a high degree of homogeneity. The average chemical composition of the samples after SPS is presented in Table 3.

**Table 3.** Chemical composition of samples after SPS

| Composition | Al, wt.% | Si, wt.% | Cr, wt.% | Fe, wt.% | Co, wt.% | Ni, wt.% |
|---|---|---|---|---|---|---|
| AlCrFeCoNi | 11.57 | - | 20.48 | 22.50 | 24.30 | 21.15 |
| $AlCrFeCoNiSi_{0.01}$ | 11.26 | 0.07 | 20.38 | 21.48 | 23.18 | 23.63 |

The measured density values were 7.292 g/cm$^3$ for the base AlCrFeCoNi alloy and 7.084 g/cm$^3$for the Si-modified $AlCrFeCoNiSi_{0.01}$ alloy. The observed decrease in density upon silicon addition is consistent with the low intrinsic density of silicon (2.33 g/cm$^3$) relative to the heavy transition metals in the matrix.

Microhardness measurements showed that the AlCrFeCoNi sample has a hardness of 489.7 HV, and $AlCrFeCoNiSi_{0.01}$ – 457.7 HV. The decrease in hardness upon the introduction of Si is probably due to the fact that the silicide phase is concentrated predominantly along the grain boundaries and does not make a significant contribution to the resistance to plastic deformation of the matrix. Similar results were obtained in [23], where it was shown that the uneven distribution of strengthening phases can weaken the dispersion strengthening effect.

The results of abrasive wear tests are presented in Table 4. Using the experimentally determined densities (7.292 g/cm$^3$ for the base alloy and 7.084 g/cm$^3$ for the Si-modified alloy), the total mass losses of 0.0399 g and 0.0221 g correspond to volumetric wear of approximately 5.5 and 3.1 mm$^3$, respectively. According to established literature on the ASTM G65 method [24], reliable statistical evaluation of wear requires a minimum volumetric loss of 200 mm$^3$ to overcome inherent methodological variations (e.g., rubber wheel wear, abrasive particle size distribution). Since the measured volumetric wear in this study falls significantly below this reliable detection threshold, the absolute wear

values of both compositions should be considered as lying within the measurement uncertainty of the method. Therefore, the wear resistance of the Si-modified alloy is at the level of the base alloy within the experimental error of this specific test.

**Table 4.** Volumetric and mass wear of SPS samples

| Sample | Mass loss, g (0-2000 revolutions, 1 cycle) | Mass loss, g (2000-4000 revolutions, 2 cycle) | Total mass loss, g | Volumetric wear, $mm^3$ |
|---|---|---|---|---|
| AlCrFeCoNi | 0.0228 | 0.0171 | 0.0399 | 5.5 |
| $AlCrFeCoNiSi_{0.01}$ | 0.0154 | 0.0067 | 0.0221 | 3.1 |

Nevertheless, the two-cycle test protocol reveals an indicative trend in wear dynamics. In the second cycle (steady-state regime), the wear rate of AlCrFeCoNiSi0.01 decreased by a factor of 2.3 (from 0.0154 to 0.0067 g), whereas for the base alloy the reduction was only 1.3× (from 0.0228 to 0.0171 g). This stabilization is consistent with the formation of protective tribo-oxide films and dispersion strengthening by silicide precipitates, as reported for similar HEAs systems [25–29].

To obtain coatings from the investigated compositions by the HVOF method, the powders after MA were subjected to plasma spheroidization to give better flowability to the powder by obtaining a spherical particle shape. Figure 5 shows the morphology of the powders after plasma spheroidization.

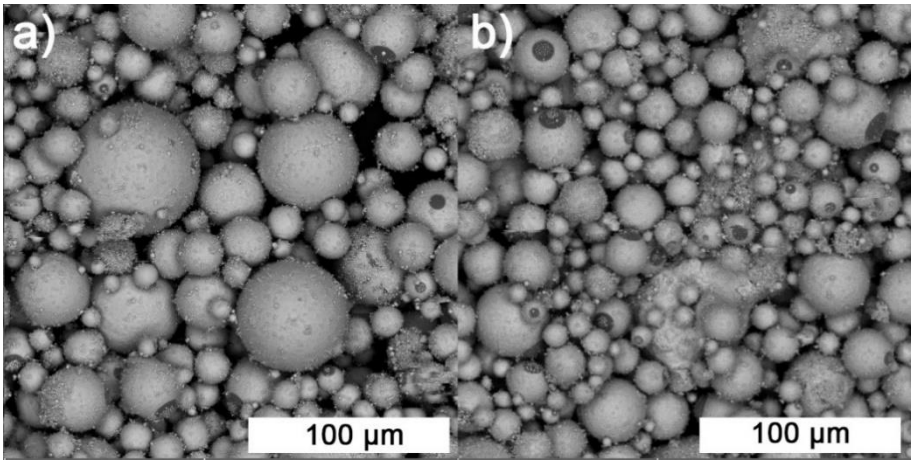



**Fig. 5.** Morphology of powders (a,b) after plasma spheroidization

The obtained powders after plasma spheroidization are characterized by a high degree of sphericity; however, a submicron fraction is present in the powder volume, which negatively affects the powder flowability and can strongly oxidize during the coating process. To remove the submicron fraction, powder classification was performed; the particle size distribution after classification for the AlCoCrFeNi composition: $d_{10}$ = 4.3 µm, $d_{50}$ = 26.6 µm, $d_{90}$ = 45.9 µm, for $AlCrFeCoNiSi_{0.01}$: $d_{10}$ = 9.4 µm, $d_{50}$ = 21.9 µm, $d_{90}$ = 42.6 µm, which ensured stable powder feeding into the spray nozzle.

Analysis of the cross-sections of the coatings (Fig. 6(a,b)) revealed the critical effect of silicon on the integrity of the layer. The AlCrFeCoNi coating (thickness of 26.8 µm) contains multiple microcracks passing along the entire "coating-substrate" interface, which indicates high residual stresses and low adhesion. In contrast, the $AlCrFeCoNiSi_{0.01}$

coating (thickness 43.3 μm) is distinguished by tight adhesion, the absence of through-cracks and pores at the interface. It can be assumed that silicon, forming low-melting eutectics or glassy silicate phases during high-temperature impact, acts as an active flux, improving the wettability of the substrate and relaxing thermal stresses.

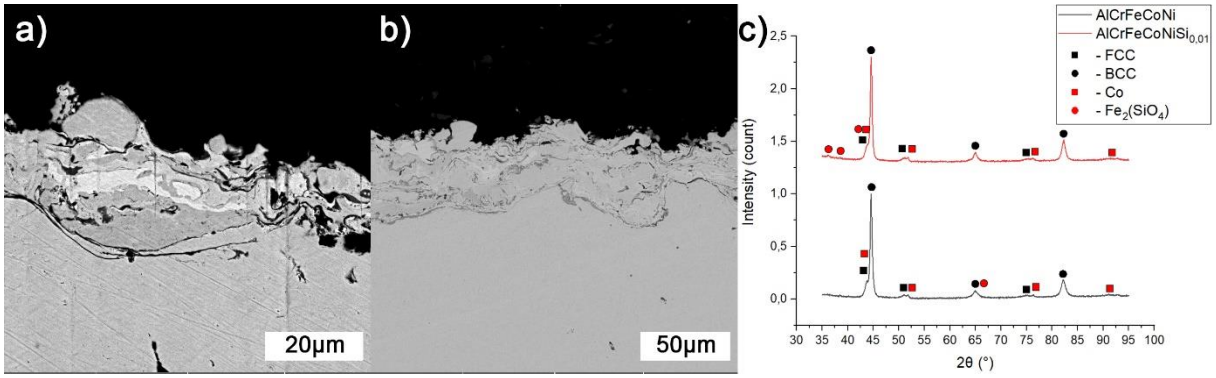



**Fig. 6.** Microstructure of coatings: (a) AlCrFeCoNi, (b) $AlCrFeCoNiSi_{0.01}$, (c) X-ray diffraction pattern of coatings

EDS analysis (Table 5) showed that during the HVOF spraying process, both alloys undergo burnout of easily oxidized elements (Al and Cr), which is confirmed by the relative increase in the concentration of Co and Ni. However, in the coating with silicon, the Cr content was 17.64 wt. %, which is significantly higher than in the coating without Si (14.16 wt. %). Silicon was not detected in the coating. This apparent contradiction with the X-ray diffraction data (Fig. 6(c)), which clearly identifies the $Fe_2(SiO_4)$ compound, is attributed to the known limitations of standard EDS analysis for light elements in heavy metal matrices. Silicon often forms amorphous or glassy silicate films, or nanoscale precipitates that fall below the EDS detection limit or are masked by X-ray absorption effects. XRD, being highly sensitive to the crystalline structure of specific phases, successfully detects the crystalline $Fe_2(SiO_4)$ formed as a result of high-temperature interaction in the flame.

**Table 5.** Comparison of chemical composition

| Sample | Al, wt. % | Si, wt. % | Cr, wt. % | Fe, wt. % | Co, wt. % | Ni, wt. % |
|---|---|---|---|---|---|---|
| AlCrFeCoNi powder | 10.73 | - | 20.22 | 24.01 | 23.71 | 21.34 |
| AlCrFeCoNi coating | 10.27 | - | 14.16 | 23.90 | 26.27 | 25.41 |
| $AlCrFeCoNiSi_{0.01}$ powder | 10.93 | 0.21 | 20.47 | 22.15 | 23.36 | 22.60 |
| $AlCrFeCoNiSi_{0.01}$ coating | 9.31 | - | 17.64 | 20.64 | 26.74 | 25.67 |

This fact indicates a mechanism of preferential oxidation: silicon has a higher affinity for oxygen at spraying temperatures and oxidizes first, forming a protective layer of $SiO_2$ / silicates, which diffusion-shields chromium from oxidative degradation. Similar results on the control of oxidation through composition control were obtained in [30]. X-ray phase analysis of the coatings (Fig. 6(c)) confirms that the uniform two-phase region characteristic of SPS disappears, the FCC phase peaks broaden due to high microstrains during rapid cooling, and in the $AlCrFeCoNiSi_{0.01}$ composition, the $Fe_2(SiO_4)$ compound is identified, which probably formed as a result of high-temperature interaction in the flame.

## Conclusions

Optimization of the mechanical alloying regime showed that to achieve a homogeneous composition and unimodal particle distribution, 7.5 h of MA (with the addition of isopropanol) is sufficient for the AlCrFeCoNi alloy, whereas for the silicon-modified $AlCrFeCoNiSi_{0.01}$ alloy, the process requires an increase in time to 10 h due to slowed diffusion. Spark plasma sintering of powders made it possible to obtain a two-phase structure (BCC + FCC). The addition of 0.11 wt. % Si stimulates the precipitation of the silicide phase ($Al_9Fe_2Si_2$) along grain boundaries.

Preliminary abrasive wear testing (ASTM G65) revealed that the volumetric wear of both SPS compositions (~ 5.5 and ~ 3.1 $mm^3$) falls below the reliable detection threshold of the method (~ 200 $mm^3$); thus, the wear resistance of the Si-modified alloy is at the level of the base alloy within experimental uncertainty. However, the observed wear-rate dynamics suggest a tendency for surface stabilization during the steady-state cycle, hypothesized to be driven by the formation of protective tribo-oxide films. Microhardness measurements showed that the AlCrFeCoNi sample has a hardness of 489.7 HV, and $AlCrFeCoNiSi_{0.01}$ – 457.7 HV.

During HVOF spraying, silicon acts as an effective modifier. Its preferential oxidation shields chromium from burnout (the Cr concentration in the coating increases from 14.16 to 17.64 % compared to the silicon-free counterpart) and promotes the formation of a glass phase, which radically improves the adhesion of the coating to the substrate, eliminating through-cracking. A comprehensive study proves that silicon microalloying is a highly effective strategy for improving the tribological characteristics and technological efficiency of applying coatings from HEAs of the AlCrFeCoNi system by gas-flame spraying.

## CRediT authorship contribution statement

**Ekaterina V. Volokitina**: writing – original draft, investigation; **Dmitriy V. Masaylo**: writing – review & editing, conceptualization; **Artem E. Kim**: writing – original draft, investigation; **Anatoliy A. Popovich**: supervision, data curation.

## Conflict of interest

The authors declare that they have no conflict of interest.

## References

1. Zhang X, Yang Z. Molecular Dynamics Study on Wear Resistance of High Entropy Alloy Coatings Considering the Effect of Temperature. *Materials.* 2024;17(16): 3911.
2. Pickering EJ, Jones NG. High-entropy alloys: a critical assessment of their founding principles and future prospects. *International Materials Reviews.* 2016;61(3): 183–202.
3. Odetola PI, Babalola BJ, Afolabi AE, Anamu US, Olorundaisi E, Umba MC, Phahlane T, Ayodele OO, Olubambi PA. Exploring high entropy alloys: A review on thermodynamic design and computational modeling strategies for advanced materials applications. *Heliyon.* 2024;10(22): 39660.
4. George EP, Curtin WA, Tasan CC. High entropy alloys: A focused review of mechanical properties and deformation mechanisms. *Acta Materialia.* 2020;188: 435–474.
5. Jiang F, Ai G, Si F, Liu J, Wei N, Wang J. Research Progress of the Effect of Alloy Composition on the Wear Resistance of High-entropy Alloy Coatings. *China Surface Engineering.* 2024;37(4): 18–43.

6. Lach L. Phase Stability and Transitions in High-Entropy Alloys: Insights from Lattice Gas Models, Computational Simulations, and Experimental Validation. *Entropy.* 2025;27(5): 464.
7. Evans D, Chen J, Bokas G, Chen W, Hautier G, Sun W. Visualizing temperature-dependent phase stability in high entropy alloys. *npj Computational Materials.* 2021;7: 151.
8. Saitova RR, Arutyunyan AR. Creep and long-term strength of high-entropy alloys. *Materials Physics and Mechanics.* 2025;53(3): 116–121.
9. Peivaste I, Jossou E, Tiamiyu AA. Data-driven analysis and prediction of stable phases for high-entropy alloy design. *Scientific Reports.* 2023;13: 22556.
10. Liang F, Du J, Su G, Xu C, Zhang C, Kong X. Phase Stability and Mechanical Properties Analysis of AlCoxCrFeNi HEAs Based on First Principles. *Metals.* 2022;12(11); 1860.
11. Liu J, Bai M, Xu W, Chu T. Effect of Processing Parameters on the Microstructure and Corrosion Properties of AlCrFeCoNi High-Entropy Alloy Coatings Fabricated by Laser Cladding. *Metals.* 2025;15(3): 231.
12. Wu M, Yuan J, Diao G, Li D. Achieving a Combination of Higher Strength and Higher Ductility for Enhanced Wear Resistance of $AlCrFeNiTi_{0.5}$ High-Entropy Alloy by Mo Addition. *Metals.* 2022;12(11): 1910.
13. Yuan Z, Yang Z, Lu Y, Yuan T, Tu Y, Ni Z, Wei L, Raza SRA. Microstructure characterization and corrosion resistance of eutectic and near-eutectic AlCoCrFeNi high-entropy alloys. *Journal of Materials Research and Technology.* 2025;36: 8367–8379.
14. Uporov SA, Ryltsev RE, Bykov VA, Zamyatin S. Microstructure, phase formation and physical properties of AlCoCrFeNiMn high-entropy alloy. *Journal of Alloys and Compounds.* 2020;820: 153228.
15. Han Y, Fu H. Improvement of High Temperature Wear Resistance of Laser-Cladding High-Entropy Alloy Coatings: A Review. *Metals.* 2024;14(9): 1065.
16. Xiang D, Liu Y, Yu T, Wang D, Leng X, Wang K, Liu L, Pan J, Yao S, Chen Z. Review on wear resistance of laser cladding high-entropy alloy coatings. *Journal of Materials Research and Technology.* 2024;28: 911–934.
17. Naseri M, Moghaddam AO, Shaburova N, Mikhailov D, Gholami D, Mourad AHI, Pellenen A, Trofimov E. Upgrading the strength-ductility trade-off and wear resistance of $Al_{0.25}CoCrFeNiCu$ and $Al_{0.45}CoCrFeNiSi_{0.45}$ high-entropy alloys through severe cold rolling process. *Materials Today Communications.* 2024;38: 1080365.
18. Zirari T, Trabadelo V. A review on wear corrosion and wear-corrosion synergy of high entropy alloys. *Heliyon.* 2024;10(4): 25867.
19. Oketola AM, Adegbola TA, Jamiru T, Ogunbiyi O, Salifu S. Advances in High-Entropy Alloy Research: Unraveling Fabrication Techniques, Microstructural Transformations, and Mechanical Properties. *Journal of Bio Tribo Corrosion.* 2025;11: 79.
20. Syundyukov IS, Skotnikova MA, Ryabikin AYu. Ultrasonic layer-by-layer treatment of PN85Y15 coating as a way to increase wear resistance of friction pair with bronze. *Materials Physics and Mechanics.* 2024;52(4): 52–62.
21. Meijun L, Xu L, Zhu C, Li Z, Wei S. Research progress of high entropy alloy: Surface treatment improves friction and wear properties. *Journal of Materials Research and Technology.* 2024;28: 752–773.
22. Feltrin AC, Xing Q, Akinwekomi AD, Waseem OA, Akhtar F. Review of Novel High-Entropy Protective Materials: Wear, Irradiation, and Erosion Resistance Properties. *Entropy.* 2022;25(1): 73.
23. Chen S, Qi C, Liu J, Zhang J, Wu Y. Recent Advances in W-Containing Refractory High-Entropy Alloys—An Overview. *Entropy.* 2022;24(11): 1553.
24. Doering D, Danks S, Mahmoud J, Scott D. Evaluation of ASTM G65 abrasive wear test — Spanning 13 years of sand. *Wear.* 2011;271(9–10): 1252–1257.
25. Feng C, Wang X, Yang L, Guo Y, Wang Y. High Hardness and Wear Resistance in AlCrFeNiV High-Entropy Alloy Induced by Dual-Phase Body-Centered Cubic Coupling Effects. *Materials.* 2022;15(19): 6896.
26. Hamdi H, Abedi HR, Zhang Y. Study on Outstanding High-Temperature Wear Resistance of High-Entropy Alloys. *Advanced Engineering Materials.* 2023;25: 2201915.
27. Vignesh M, Sujit M, Radhika N, Sathishkumar M, Muthu SM, Dash K, Mishra SR. Influence of Cu and Co addition on metallurgical and wear characteristics of AlCrFeNi high entropy alloy. *Scientific Reports.* 2024;14: 27398.
28. Naseri M, Moghadam AO, Anandkumar M, Sudarsan S, Bodrov E, Samodurova M, Trofimov E. Enhancing the mechanical properties of high-entropy alloys through severe plastic deformation: A review. *Journal of Alloys and Metallurgical Systems.* 2024;5: 10054.
29. Li R, Yu W, Zhang Y, Li C, Qu Y, Nie S, Tian C, Tan B, Yu B. Effect of Phase Proportion on Wear Behavior of Al–Cr–Fe–Ni Dual-Phase High Entropy Alloys. *Metallography, Microstructure, and Analysis.* 2021;10: 106–115.
30. Xu J, Kong X, Chen M, Wang Q, Wang F. High-entropy FeNiCoCr alloys with improved mechanical and tribological properties by tailoring composition and controlling oxidation. *Journal of Materials Science & Technology.* 2021;82: 207–213.